A Search for TeV Gamma-ray Emission from the PSR B1259−63/SS2883 Binary System with the CANGAROO-II 10-m Telescope

A. Kawachi[1], T. Naito[2], J.R. Patterson[3], P.G. Edwards[4], A. Asahara[5], G.V. Bicknell[6], R.W. Clay[3], R. Enomoto[1], S. Gunji[7], S. Hara[1,5], T. Hara[2], T. Hattori[8], Sei. Hayashi[9], Shin. Hayashi[9], C. Itoh[10], S. Kabuki[1], F. Kajino[9], H. Katagiri[1], T. Kifune[11], L. Ksenofontov[1], H. Kubo[5], J. Kushida[5,12], Y. Matsubara[13], Y. Mizumoto[14], M. Mori[1], H. Moro[8], H. Muraishi[15], Y. Muraki[13], T. Nakase[8], D. Nishida[5], K. Nishijima[8], M. Ohishi[1], K. Okumura[1], R.J. Protheroe[3], K. Sakurazawa[12], D.L. Swaby[3], T. Tanimori[5], F. Tokanai[7], K. Tsuchiya[1], H. Tsunoo[1], T. Uchida[1], A. Watanabe[7], S. Watanabe[5], S. Yanagita[10], T. Yoshida[10], and T. Yoshikoshi[16]

kawachi@icrr.u-tokyo.ac.jp

ABSTRACT

[1] Institute for Cosmic Ray Research, University of Tokyo, Kashiwa, Chiba 277-8582, Japan

[2] Faculty of Management Information, Yamanashi Gakuin University, Kofu, Yamanashi 400-8575, Japan

[3] Department of Physics and Mathematical Physics, University of Adelaide, SA 5005, Australia

[4] Institute of Space and Astronautical Science, Sagamihara, Kanagawa 229-8510, Japan

[5] Department of Physics, Graduate School of Science, Kyoto University, Sakyo-ku, Kyoto 606-8502, Japan

[6] Research School of Astronomy and Astrophysics, Australian National University, ACT 2611, Australia

[7] Department of Physics, Yamagata University, Yamagata, Yamagata 990-8560, Japan

[8] Department of Physics, Tokai University, Hiratsuka, Kanagawa 259-1292, Japan

[9] Department of Physics, Konan University, Kobe, Hyogo 658-8501, Japan

[10] Faculty of Science, Ibaraki University, Mito, Ibaraki 310-8512, Japan

[11] Faculty of Engineering, Shinshu University, Nagano, Nagano 480-8553, Japan

[12] Department of Physics, Tokyo Institute of Technology, Meguro, Tokyo 152-8551, Japan

[13] Solar-Terrestrial Environment Laboratory, Nagoya University, Nagoya, Aichi 464-8602, Japan

[14] National Astronomical Observatory of Japan, Mitaka, Tokyo 181-8588, Japan

[15] Ibaraki Prefectural University of Health Sciences, Ami, Ibaraki 300-0394, Japan

[16] Department of Physics, Osaka City University, Osaka, Osaka 558-8585, Japan

Observations of the PSR B1259−63/SS2883 binary system using the CANGAROO-II Cherenkov telescope are reported. This nearby binary consists of a 48 msec radio pulsar in a highly eccentric orbit around a Be star, and offers a unique laboratory to investigate the interactions between the outflows of the pulsar and Be star at various distances. It has been pointed out that the relativistic pulsar wind and the dense mass outflow of the Be star may result in the emission of gamma rays up to TeV energies. We have observed the binary in 2000 and 2001, ∼47 and ∼157 days after the October 2000 periastron. Upper limits at the 0.13–0.54 Crab level are obtained. A new model calculation for high-energy gamma-ray emission from the Be star outflow is introduced and the estimated gamma-ray flux considering Bremsstrahlung, inverse Compton scattering, and the decay of neutral pions produced in proton-proton interactions, is found to be comparable to the upper limits of these observations. Comparing our results with these model calculations, the mass-outflow parameters of the Be star are constrained.

Subject headings: binaries: close—gamma rays: observations, theory— stars: winds, outflows

1. Introduction

PSR B1259−63 ((α, δ)(J2000) = ($13^h02^m47^s.68$, $-63°50'08''.6$)) is a 48 msec radio pulsar discovered in a 1500 MHz radio survey of the southern Galactic plane (Johnston et al. 1992a) which was subsequently found to be in a highly eccentric orbit with a 10th magnitude main-sequence star, SS 2883 (Johnston et al. 1992b, 1994). With an orbital eccentricity of 0.87, the separation of the stars varies in the range $0.97\sim14.0\times10^{13}$cm during the orbital period of 1236.72 days. The periastron epoch is MJD 48124.35 (Wex et al. 1998). SS 2883 is of spectral type B2e (Johnston et al. 1994), with a mass M_* of $\sim10\,M_\odot$ and a radius R_* of $\sim6\,R_\odot$. The luminosity and radius of the B2e star correspond to an effective temperature $T_{\rm eff}$ of ∼27,000 K at the star surface (Tavani & Arons 1997). Its characteristic emission disc extends to at least $20\,R_*$, similar to the distance between the pulsar and the Be star at periastron. Here we assume a distance of 1.5 kpc to the binary system, which has been estimated from optical photometric observations of SS 2883 (Johnston et al. 1994).

The periastron passages have been closely observed at radio frequencies (Johnston et al. 1999; Connors et al. 2002). No pulsed emission was detected for about five weeks centered on periastron and the pulsed emission was depolarized for ∼200 days also centered on periastron. Timing measurements have shown that the disc of the Be star is likely to be inclined with

respect to the orbital plane (Melatos, Johnston & Melrose 1995; Wex et al. 1998), which has been suggested in Kaspi et al. (1995); Tavani & Arons (1997). In Connors et al. (2002), the unpulsed light curves are discussed with an assumption of two short-time crossings of the pulsar and the disc, before [(τ−18 d) ∼ (τ−8 d)] and after [(τ+12 d) ∼ (τ+22 d)] periastron (τ).

A weak X-ray signal was first detected by *ROSAT* which observed the system just after apastron in September 1992 (Cominsky, Robers, & Johnston 1994). Through 1994–1996, unpulsed X-ray emission with a single power-law spectrum was detected at the six different orbital phases observed by *ASCA* (Hirayama et al. 1996, 1999). The photon index of the X-ray spectrum is about −1.6 in the post-periastron to apastron period, steepening towards periastron where the steepest index of −1.96 was observed. The 1–10 keV band luminosity varies by about an order of magnitude, from $\sim 10^{34}$ ergs s^{-1} around periastron to $\sim 10^{33}$ ergs s^{-1} at apastron. The maximum luminosity was detected at τ−12 d, with the intensity decreasing at periastron, then increasing again. The column density was low and constant (6×10^{21}cm^{-2}) at all orbital phases. The periastron passage in January 1994 was monitored by a multi-wavelength campaign including observations in the X-ray and gamma-ray bands with *ROSAT*, *ASCA* and *CGRO* (Grove et al. 1995). The power-law spectrum (photon index ∼ −2.0) extended to the 200 keV energy region of *OSSE*, with no pulsations being detected. No emission in the energy range of 1 MeV–3 GeV was detected down to the observational limits. *OSSE* failed to detect signals at the apastron passage in 1996, however, its upper limit does not conflict with the extrapolation of the *ASCA* spectrum (Hirayama et al. 1999). Several TeV observations of the binary system were performed in 1994 and 1997 using the CANGAROO 3.8-m ground-based Cherenkov telescope, resulting in a marginally significant suggestion of gamma-ray signals (Sako et al. 1997).

The multi-wavelength spectrum from the 1994 periastron strongly implies that the hard X-ray emission up to 200 keV originates from synchrotron radiation of non-thermal electrons (Tavani, Arons & Kaspi 1994). Electrons released in the pulsar wind may be accelerated in a shock wave generated in the region where the relativistic pulsar wind interacts with dense mass flow from the Be star. Adjusting the pressure balance between the flows, Tavani & Arons (1997) have interpreted the measured hard X-ray spectrum on the basis of accelerated particles in the pulsar-side shock, using an approximated approach to the Klein-Nishina effect for emission. They conclude that the energy loss of electrons due to inverse Compton scattering is dominant, and that the Lorentz factor of accelerated electrons is $\Gamma_e = 10^6 - 10^7$. Accretion onto the neutron star is unlikely to be significant, as there is an absence of X-ray/gamma-ray pulsations, an absence of the day–scale fluctuations in X-rays, a relatively low X-ray luminosity, and negligible absorption as a result of the low column density. The consistency of the X-ray luminosities at the same orbital phases in

different years supports the idea that the observed time variability is due to binary modulation (Hirayama et al. 1999; Kaspi 1997). Recently, another model for the pulsar-side shock considering the Klein-Nishina effect in the emission and cooling process has been proposed. Murata et al. (2003) note that the inverse Compton cooling dominated spectrum is flatter, since the Klein-Nishina effect suppresses the cooling of higher-energy electrons. It is argued that synchrotron cooling, instead of the inverse Compton scattering discussed by Tavani & Arons (1997), is the dominant process for the energy loss of electrons in the pulsar wind on the account of the steepening of the X-ray spectral index observed around the 1994 periastron.

The light curves of the radio unpulsed emission around periastron have been recently modeled by the adiabatic expansion of synchrotron bubbles formed in the pulsar and the Be star disc interaction (Connors et al. 2002). They assume short-time interactions of the pulsar and the disc, as the pulsar should cross the disc twice in the orbital period. When the pulsar enters the disc, electrons are accelerated in the contact surface of the pulsar wind and the disc material, but after the pulsar leaves the disc, the pulsar-wind bubble remains behind, moves in the disc-flow, and decays through synchrotron losses. The model successfully explains the radio data, however, it does not appear to describe the X-ray data well; for example, the weak unpulsed emissions in the X-ray region was observed after these modeled bubbles should have decayed by adiabatic expansion as moving outwards, and, the constant spectral index in the radio region is inconsistent with the steepening observed in the X-ray spectrum.

Electrons accelerated in a pulsar-side shock to Lorentz factors of $\Gamma_e \gtrsim 10^6$ in the radiative environment of the binary system may produce high energy gamma rays. The suggestion that detectable levels of gamma-ray emission may arise in the shocked pulsar wind via inverse Compton scattering (Kirk, Ball & Skjaeraasen 1999) provided the initial motivation for the observations described here. Subsequently, inverse Compton emission from the un-shocked region of the pulsar wind has been considered (Ball & Kirk 2000; Ball & Dodd 2001). The integrated contribution from the un-shocked pulsar wind may increase the gamma-ray flux around periastron for some conditions. The maximum level of emission in the TeV energy range is estimated to be $\sim 4 \times 10^{-5}\mathrm{MeVcm}^{-2}\mathrm{s}^{-1}$ in the integrated energy flux with a wind Lorentz factor of 10^7 (Ball & Kirk 2000) which may raise the TeV gamma-ray flux above our detector's sensitivity of typically $10^{-11} - 10^{-12}\mathrm{TeVcm}^{-2}\mathrm{s}^{-1}$. Further studies have considered the effect of the termination of the wind (Ball & Dodd 2001), which, depending on its assumped location, may act to decrease the inverse Compton flux compared to previous predictions. On the other hand, Murata et al. (2003) predict a maximum energy flux from the pulsar wind of $\sim 10^{-13}\mathrm{erg\,s}^{-1}\mathrm{cm}^{-2}$ at TeV energies around periastron, which would require a very deep observation to detect.

At the contact surface of the pulsar and Be star flows, ions and electrons in the Be star outflow may be accelerated to high energies via the first-order Fermi mechanism. In the dense outflow from the Be star there is a lot of target material for proton-proton interactions and Bremsstrahlung emission. The Be star also provides target photons for upscattering by the inverse Compton mechanism, in addition to the 2.7 K microwave background radiation. The densities of these targets increase as the contact surface gets closer to the Be star, and so does the total energy of accelerated particles. In this paper, a new model calculation for gamma-ray emission from the accelerated particles in the Be star outflow, taking into consideration Bremsstrahlung, the inverse Compton mechanism, and proton-proton interactions, is applied to the binary system and discussed along with our observational results.

2. Observations

The CANGAROO (*C*ollaboration between *A*ustralia and *N*ippon for a *GA*mma-*R*ay *O*bservatory in the *O*utback) Cherenkov telescopes are located near Woomera, South Australia (136°47′E, 31°06′S, 160m a.s.l.). The 3.8-m CANGAROO telescope, used for the previous observations of PSR B1259−63, was operated from 1991 to 1998. The CANGAROO-II telescope was constructed in 1999 initially with a 7-m diameter dish, which was upgraded to 10-m in 2000 (Mori et al. 2001). Cherenkov photons from extensive air showers which are initiated by primary gamma-rays/cosmic rays are collected with a parabolic reflector and detected by an imaging camera placed in the prime focal plane. The 10-m reflector consists of 114 spherical plastic mirrors of 0.8 m diameter (Kawachi et al. 2001) to make a composite parabolic shape ($f/0.8$). The camera has an array of 552 photomultiplier tubes (PMTs) of half-inch diameter (Hamamatsu, R4124UV) covering a field-of-view of 2.8°, with groups of 16 PMTs using the same high voltage line. In the observations described in this paper, accepted events were required to meet two conditions within the central region of the camera (1° diameter); at least three PMTs above a ∼3-photoelectron threshold, and at least one preamplifier unit with an analogue sum of signals above a ∼10-photoelectron threshold. The typical raw trigger rates of these observations were in the 10–80 Hz range. The charge and timing information of each PMT signal was recorded for each event. Details of the telescope are given in Mori et al. (2001) and Asahara et al. (2003).

The PSR B1259−63/SS2883 system was observed with the CANGAROO-II Cherenkov telescopes at two different orbital phases; for several days in December 2000 (hereafter *Obs. A*; MJD 51881.4 in average of the observation time) and in March 2001 (*Obs. B*; MJD 51991.5), about 47 and 157 days after the periastron of October 2000 (MJD 51834.51). The orbital phase of *Obs. A* is similar to the *ASCA* Obs. 4 in Hirayama et al. (1999). We have no data

closer to periastron as observing conditions were not suitable during June–November 2000. The orbital phases of the observations are schematically shown in Figure 1, and details of the observations are summarized in Table 1. In all observations the telescope was pointed so that the binary system was at the tracking center.

The target and offset region(s) were observed for equal amounts of time on each night under moonless and fine sky conditions. In a typical observation, the target (ON-source) region was observed for a few hours including source culmination, and an offset (OFF-source) run was carried out before and/or after the ON-source run to cover the same track, in the elevation and azimuthal angles, as that of the ON-source run. The average zenith angles were 58° for *Obs. A* and 34° for *Obs. B*, corresponding to differences in observing seasons. The observations closer to periastron, *Obs. A*, were performed at larger zenith angles, thus at a higher energy threshold, than the optimum observing condition for the source. The zenith angle of 58° is similar to the observing conditions for the Crab nebula (∼55° in Tanimori et al. (1998)) from the CANGAROO site, thus the data has been analyzed in a similar manner to the recent analysis of the Crab data (Itoh et al. 2003).

3. Analysis and Results

3.1. Data Analysis

The digitized counts of PMT signal charges have been calibrated after pedestal subtraction. The gains of the pixels have been normalized using a blue LED located at the center of the telescope to illuminate the camera uniformly. The LED is driven by a fast pulse generator. Accidental events, caused mainly due to the night sky or environmental background light, have been removed in the analysis by requiring at least five neighboring PMTs to exceed the ∼3.3 photoelectron threshold within ±35 nsec. A small number of pixels affected by noise or the passage of bright stars have been excluded from the analysis. The count rate of events which satisfy these criteria is stable (about 0.6 Hz and 1.9 Hz in *Obs. A* and *Obs. B* data sets, respectively), and differences in the raw event rates between ON- and OFF-source runs, ratios of about 1:4 in *Obs. A* and 3:2 in *Obs. B*, respectively, have been resolved. Data under cloudy or unstable conditions have been rejected by checking deviations of the counting rate. The effective observation time and event numbers at this stage of the analysis are summarized in Table 2.

In order to discriminate gamma-ray events from cosmic-ray induced events, a likelihood analysis has been applied (Enomoto et al. 2002b; Itoh et al. 2003) to the characteristic light images recorded by the camera. In this image-analysis, we also require the total charge con-

tained in an image to be greater than ∼35 photoelectrons, in order to improve the efficiency of background rejection. We have used Monte Carlo simulations (Enomoto et al. 2002a) for a gamma-ray (γ) event set and the OFF-source events for the background (BG) event set. The average zenith angle, the discarded pixels, and the cut parameters in the analysis have been taken into account in the simulations for the different conditions of *Obs. A* and *Obs. B*. The following results are based on simulations assuming a power-law energy spectrum with an index of -2.5 for the generated gamma-rays. The "hit-map" of triggered pixels, weighted by size of the signal, has been fitted with an ellipse parametrized by the r.m.s. spread of light along the minor/major axis of the image ($width/length$), and the distance between the image centroid and the source position ($distance$) (Hillas 1982) to characterize each event. Images truncated by the camera edge, or too concentrated at the camera center, have been omitted by putting a loose limit on $distance$ ($0.35^\circ \leq distance \leq 1.2^\circ$). Each of the image parameters have been plotted against the total signal in the image for the γ and BG event sets to produce probability density functions (PDF) of the "γ-like" and "BG-like" events, respectively. Thus the dependences of the image parameters on the event size have been taken into the analysis. Finally, a single parameter, $R_{prob} = Prob(\gamma)/[Prob(\gamma) + Prob(BG)]$, is calculated for each event, where $Prob(\gamma)[Prob(BG)]$ is the probability of the event being due to a γ $[BG]$, calculated from the two-dimensional PDFs. We use the PDFs of three parameters with equal weight. A selection criteria (R =0.4; $R_{prob} \geq R$) has been chosen considering the acceptance of γ events and the figure-of-merit of γ events to the BG events. The event numbers of the selected data are listed in Table 2.

After the image selection, gamma-rays from the pulsar should have the image orientation parameter *alpha* (Punch et al. 1992) less than 20° for the *Obs. A* data set, and 15° for the *Obs. B* set. A broader *alpha* distribution for gamma-rays at larger zenith angle is expected from simulations (Okumura et al. 2002). Figure 2 shows the distributions of *alpha* after all the other cuts have been applied. The OFF-source ("OFF") *alpha* distributions are normalized to that of the ON-source ("ON") by the number of events with $alpha \geq 40^\circ$. The normalization factor is consistent with that deduced from the effective observation times, within statistical errors. No statistically significant excess of the "ON" over the "OFF" is seen in either of the *alpha* histograms. Subtracting the normalized "OFF" counts from the "ON" data results in 31 and 47 events within the *alpha* selection criteria, corresponding to the significances (assuming Poisson fluctuations only) of $+1.0\sigma$ and $+0.60\sigma$, for *Obs. A* and *Obs. B* respectively.

3.2. Energy Threshold and Upper Limit Flux

The gamma-ray acceptance for the cuts used in the analysis has been estimated based on the simulations. The energy threshold is defined as the peak of the acceptance multiplied by the generated energy spectrum, and thresholds of 3.6 TeV and 0.78 TeV are derived for a $E^{-2.5}$ spectrum for the *Obs. A* and *Obs. B* data sets, respectively. The corresponding effective areas are 3.6×10^9 cm^2 and 1.3×10^9 cm^2. The 2σ upper limits of our result are

$$F(\geq 3.6TeV) \leq 1.4 \times 10^{-12}\mathrm{cm}^{-2}\mathrm{s}^{-1} \quad (Obs.\, A)$$

and

$$F(\geq 0.78TeV) \leq 3.1 \times 10^{-12}\mathrm{cm}^{-2}\mathrm{s}^{-1} \quad (Obs.\, B).$$

Figure 3 shows the upper limits of the two observations. The integral flux of the Crab nebula is also shown (Tanimori et al. 1998) as a reference. The systematic error in the energy scale determination has been estimated to be 15 percent (Itoh et al. 2003) and is shown in the figure as errors in the abscissa.

The whole procedure of the analysis has been performed changing the simulated spectral index from -2.5 to -2.0. The significance levels of the gamma-ray signals are unchanged, and the corresponding threshold energies and the gamma-ray acceptances increase by about 20 percent. Thus the upper limits assuming a spectral index of -2.0 are; $F(\geq 4.0TeV) \leq 1.2\times10^{-12}\mathrm{cm}^{-2}\mathrm{s}^{-1}$ (*Obs. A*) and $F(\geq 0.88TeV) \leq 2.7\times10^{-12}\mathrm{cm}^{-2}\mathrm{s}^{-1}$ (*Obs. B*), respectively, as shown in Figure 3.

4. Discussion

The observational results are compared with some model calculations. A new model of gamma-ray emissivity is introduced, considering the particles accelerated in the Be star outflow.

4.1. Models of the two flows

Figure 4 schematically illustrates the assumed configuration of the system: the pulsar and its relativistic pulsar wind, the Be star and its polar and disc-like outflows, and the shock composed of three surfaces: pulsar-side shock, contact surface, and Be-star-side shock.

Particles are assumed to be accelerated by the shock at the pressure balance between the flows of the two stars. In the figure, the contact discontinuity between the pulsar wind and the equatorial disc of the Be star is illustrated. The alignment of the Be star disc to the orbital plane, and its effect, will be discussed later in calculating light curves over orbital phase.

For the pulsar wind, we adopt the model of Kennel & Coroniti (1984) for the synchrotron nebula around the Crab pulsar. For the Be star mass-flow, the simple model of Waters (1986) is used, which represents radiations from Be stars using the IR, optical, and UV observational results. The parameters are chosen so as to be consistent with the observational results of Be stars in general (Cote & Waters 1987) and of the PSR B1259−63/SS2883 binary (Johnston et al. 1994, 1996; Melatos, Johnston & Melrose 1995). We fully consider the Klein-Nishina effect in the calculations of the emission processes via electrons. Provided the pulsar wind is driven by the spin down luminosity ($\dot{E}_{\rm rot}$) of the pulsar, a fraction ($f_{\rm pw} = 0.1$) of the wind luminosity is assumed to be enhanced in the equatorial plane. Both kinetic and electromagnetic energies are included in $\dot{E}_{\rm rot}$ (Kennel & Coroniti 1984). The radial distribution of the wind pressure, $P_{\rm pw}$, is given by

$$P_{\rm pw}(r) = \frac{\dot{E}_{\rm rot}}{f_{\rm pw} 4\pi r^2 c} \quad , \tag{1}$$

where r is the distance from the pulsar and c is the speed of light.

For the mass-flow of the Be star, we consider a high-density, slow, equatorially orbiting disc-like flow (Waters 1986), and a low-density, fast, polar component (stellar wind) (Waters et al. 1988; Dougherty et al. 1994) as well. The density profile, ρ, is assumed to depend on the distance from the center of the Be star, R, as $\rho(R) = \rho_0 (R/R_*)^{-n}$ with a power-law index n, where R_* is the star radius and ρ_0 is the density of the outflow at the surface of the star. The flow speed $v(R) = v_0 (R/R_*)^{n-2}$ is obtained from conservation of mass flux, where v_0 is speed of the outflow at the surface of the star. Then the momentum flux of the flow, $P_{\rm Be}$, is

$$P_{\rm Be}(R) = \rho v^2 = \rho_0 v_0^2 (\frac{R}{R_*})^{n-4}. \tag{2}$$

In our calculation, indices n of 2.5 and 2 are chosen in outflows of disc and polar wind, respectively.

The location of the shock regime is determined by the balance between pressures of the pulsar wind (Eq. 1) and of the Be star outflow (Eq. 2).

We introduce a new parameter, x, defined as

$$x = \frac{\rho_0}{10^{-12}{\rm gcm}^{-3}} \frac{v_0}{10^6 {\rm cms}^{-1}}. \tag{3}$$

When x is larger, the location of the pressure balance becomes further from the Be star. If we assume that the opening angle $\theta_{\rm disc}$ of the disc outflow is 15° (Johnston et al. 1996), the parameter x is related to the Υ of Tavani & Arons (1997) by $\Upsilon \equiv (\dot{M}/10^{-8} M_\odot \ {\rm yr}^{-1})\ (v_0/10^6 {\rm cm\ s}^{-1}) = 0.90 \times x \times (v_0/10^6 {\rm cm\ s}^{-1})$, where $\dot{M}$ is the mass loss rate. The parameter x depends on v_0 and ρ_0, which are obtained directly from UV/optical observations, independent of the disc opening angle. As shown later, the gamma-ray emission is approximately proportional to x^2 in our model.

4.2. Particle acceleration and gamma-ray spectrum

First, we deduce the flux $j_{\rm i}$ (i = e,p) as a function of energy $E_{\rm i}$ of the particles in the Be star outflow on the basis of Fermi acceleration, where e denotes electrons and p denotes protons. For simplicity, we assume that all ions are protons. Secondly, we calculate the energy flux from the binary system induced from the emission mechanisms of Bremsstrahlung, inverse Compton (electrons) and proton-proton collisions.

In general terms, the momentum spectrum dN/dP of the shock-accelerated particles is expressed as $N_0 P^{-\alpha}$ and $4\pi j$ is obtained from $v dN/dE_{\rm k}$, where $E_{\rm k}$ is the kinetic energy, described as $dN/dE_{\rm k} = dP/dE_{\rm k} dN/dP$. The constant $N_{0,{\rm i}}$ is evaluated with the following integration regarding of the energy balance at the shock location in the Be star flow;

$$\int_{m_{\rm i}c^2}^{E^{\rm max_i}} \frac{dN_{\rm i}}{dE_{\rm i}}(E_{\rm i}) dE_{\rm i} = f_{\rm acc,i} P_{\rm Be}(R_{\rm shock}), ({\rm i = e, p}), \tag{4}$$

where $R_{\rm shock}$ is the distance to the contact surface from the Be star center. We assume $f_{\rm acc,i} = 0.001$ and 0.1 is assumed for $i = e$ and p, respectively, as the efficiency of the acceleration to be consistent with an e/p ratio in cosmic ray observations (e.g. Müller et al. (1995); Baring et al. (1999)). The variation of $R_{\rm shock}$ causes the orbital modulation in the light curve. The orbital inclination to the line of sight has not been included in our calculation, as this effect is less significant in the Be star emission models than in the pulsar wind emission models. Anisotropy of the optical photons from the Be star is neglected for simplicity. Assuming Fermi acceleration, a power-law index of $\alpha = -2.0$ is taken for the proton momentum spectrum $dN_{\rm p}/dP_{\rm p}$ with an assumed compression ratio of 4.0. The spectral index of the electron momentum spectrum at the shock front does not vary much from the canonical $\alpha = -2.0$ for plausible values of pulsar wind parameters, because inverse Compton cooling in the higher energy electrons are reduced by the Klein-Nishina effect (Murata et al. 2003). In addition, synchrotron cooling does not affect the spectral index, since the magnetic-field strength on the Be-star side should be weak. We therefore assume that the electron spectral index has a constant value of $\alpha = -2.0$.

The integration is performed from the threshold energy or the particle mass, $m_{\rm e,p}c^2$, to the maximum energy of the accelerated particle $E_{\rm e,p}^{\rm max}$, which we assume here to be $\sim 10^{15}$ eV. Applying the obtained $j_{\rm e,p}(E_{\rm e,p})$, the gamma-ray spectrum from the source at the distance D is calculated. For the proton-proton collision emission mechanisms, the spectrum is calculated as

$$F_\gamma^{\rm pp}(E_\gamma) = \frac{1}{D^2}\int n_{\rm target} dV \int\int dE_\pi dE_{\rm p} \frac{2}{p_\pi} j_{\rm p}(E_{\rm p}) \frac{d\sigma_{{\rm pp}\to\pi}(E_\pi, E_{\rm p})}{dE_\pi} \tag{5}$$

where $n_{\rm target}$ stands for $\rho/m_{\rm p}$, and $E_{\rm p,\pi}$ and $p_{\rm p,\pi}$ denote the energy and momentum of protons or pions, respectively. Full descriptions of the integral limit and $\sigma_{{\rm pp}\to\pi}$ are given in Naito & Takahara (1994). The contributions of the inverse Compton (IC) and Bremsstrahlung are calculated from $j_{\rm e,p}(E_{\rm e,p})$ as

$$F_\gamma^{\rm IC,Brem}(E_\gamma) = \frac{1}{D^2}\int n_{\rm target} dV \int_{m_{\rm e}c^2}^{E_{\rm e}^{\rm max}} dE_{\rm e} j_{\rm e}(E_{\rm e}) \frac{d\sigma}{dE_\gamma}, \tag{6}$$

where $n_{\rm target} = n_{\rm photon}$ and $\frac{d\sigma}{dE_\gamma}$ is a cross section which includes the Klein-Nishina effect for inverse Compton emission, and $n_{\rm target}$ of $\rho/m_{\rm p}$ and the cross section $\frac{d\sigma}{dE_\gamma}$ of electron-proton and electron-electron interaction are used for Bremsstrahlung emission (Gaisser et al. 1998; Sturner et al. 1997). For $n_{\rm photon}$, we adopt 2.7 K CMB and $T_{\rm eff}$ = 27,000 K black body radiation from the Be star. In the spatial integration, we assume that the accelerated particles extend into the Be star outflow downstream of the shock. The contributions of different emission mechanisms are calculated with $x_{\rm disc}$ =1500 for the phase of periastron and their differential energy spectra are shown in Fig. 5 (the disc and the pulsar wind are assumed to interact at periastron in the calculation). The total gamma-ray flux is deduced as $F_\gamma(E_\gamma) = F_\gamma^{\rm Brem}(E_\gamma) + F_\gamma^{\rm IC}(E_\gamma) + F_\gamma^{\rm pp}(E_\gamma)$ and the dominant contribution is of $F_\gamma^{\rm pp}(E_\gamma)$. The inverse Compton flux in the sub-TeV energy region, expected from the pulsar-wind side (Murata et al. 2003), is comparable to $F_\gamma^{\rm IC}$ from the Be star outflows, except that the former has a break $\sim$400 GeV due to the stronger magnetic field in the pulsar wind side. After the spatial integration, the total flux is approximately expressed as

$$F_\gamma(E_\gamma, x) \propto x^2 \frac{1}{n-1} \frac{1}{R_{\rm shock}(x, n, v_0)} \quad . \tag{7}$$

$R_{\rm shock}(x, n, v_0)$ for the same orbital phase does not vary much within the parameter range discussed in the following.

The adopted model parameters are summarized in Table 3. Now we discuss the possible ranges of two parameters, x and the density profile index n. For the polar component, the value $x_{\rm polar}$ is set to be proportional to the disc component, $x_{\rm disc}$. The factor is estimated using the following two equations, $\dot{M}_{\rm polar} = 4\pi R_*^2\ \rho_{\rm polar,0}\ v_{\rm polar,0}\ (1 - \sin\theta_{\rm disc})$ and $\dot{M}_{\rm disc} =$

$4\pi R_*^2\ \rho_{\rm disc,0}\ v_{\rm disc,0}\ \sin\theta_{\rm disc}$, where the surface density, initial velocity, and mass loss rate of the disc [polar wind] flow are denoted as $\rho_{\rm disc[polar],0}, v_{\rm disc[polar],0}$, and $\dot{M}_{\rm disc[polar]}$, respectively, and $\theta_{\rm disc}$ denotes the opening angle of disc outflow. The ratio of two x parameters is

$$\frac{x_{\rm polar}}{x_{\rm disc}} = 3.49 \times 10^{-1} \frac{\dot{M}_{\rm polar}}{\dot{M}_{\rm disc}}, \tag{8}$$

assuming $\theta_{\rm disc} = 15°$(Johnston et al. 1996). From the observed intensities of the UV line (due to the polar wind) and of the IR radiation (from the disc), Lamers & Waters (1987) deduce the mass loss ratio of the two flow components as $\frac{\dot{M}_{\rm polar}}{\dot{M}_{\rm disc}}$ of 10^{-1}–10^{-4}. We take $x_{\rm polar}$ of $10^{-1} \times x_{\rm disc}$ as a rather optimistic value. The thick disc-like flow is an effective site for the production of gamma-ray emission, and makes the dominant contribution to the total intensity.

For $x_{\rm disc}$, early studies (Waters 1986; Waters et al. 1988; Dougherty et al. 1994) have estimated possible ranges of $10^5 < v_{\rm disc,0} < 10^7 {\rm cms}^{-1}$ and $10^{-13} < \rho_{\rm disc,0} < 10^{-9} {\rm gcm}^{-3}$. Thus we investigate $500 \leq x_{\rm disc} \leq 5000$ in this model analysis.

In Eq. 2, n =2 corresponds to a constant speed and n =4 corresponds to a constant ram pressure. We can approximate the polar wind with $n_{\rm polar}$ =2, since the polar wind is generally thought to reach a terminal speed within a few stellar radii. In contrast, the disc density falls rapidly with radius as the rotating material gradually accelerates outward. Ball et al. (1999) describes the disc of SS 2883 with $n_{\rm disc} \lesssim 4$, while Waters et al. (1988) gives $2 < n_{\rm disc} < 3.25$ from a general consideration of Be star discs. We adopt $n_{\rm disc}$ =2.5 here. Changing $n_{\rm disc}$ to 4 and keeping other parameters fixed reduces the emission by a factor of about 2 (Eq. 7).

There are no fixed limits for the orbital phases in which the Be star disc outflow interacts with the pulsar wind. We consider three possibilities in calculating the light curves; (i) aligned disc to the orbital plane and interaction throughout the orbit, (ii) mis-aligned disc and interaction in the ∼200-day period around periastron (τ), during which the radio emission is depolarized, or (iii) mis-aligned disc and interaction in two short periods, [(τ−18 d) ∼ (τ−8 d)] and [(τ+12 d) ∼ (τ+22 d)], as discussed in Connors et al. (2002). Eq. 7 with $x_{\rm polar}$ of $10^{-1} \times x_{\rm disc}$, suggests that the contribution from the polar-wind–pulsar-wind interaction is a factor $1.5{\times}10^{-2}$ of that from the disc–pulsar-wind interaction. The polar wind is generally assumed to interact with the pulsar wind at all orbital phases. When the disc and pulsar-wind interaction diminishes. the estimated intensity from the system is only of the polar-wind contribution, and is reduced by a factor of $\sim 10^{-2}$. We take account of (i), implying the maximum effect of the disc-pulsar wind interaction, though the disc material becomes dilute at larger distances (Eq. 2). In (ii) and (iii), we consider emissions from the pulsar-wind bubble formed in the disc flow, after the pulsar leaves the disc (Connors et al. 2002). The

bubble moves at the velocity $v_{\rm bubble}$ in the outflow and shock acceleration of particles in the flow proceeds in the contact discontinuity between the bubble and the outflow material. Emissions from the moving bubble are calculated along its trace referring to the material and momentum density profiles of the flow, by replacing $R_{\rm shock}(x, n, v_0)$ with $R_{\rm shock}(t = t_0, x, n, v_0) + v_{\rm bubble}(t - t_0)$ in Eq. 7, where t_0 denotes the time when the pulsar moves out of the disc flow. We assume an initial value of $v_{\rm bubble} = 100{\rm kms}^{-1}$ which is larger than the value used in Connors et al. (2002), $15{\rm kms}^{-1}$, but is similar to the model in Paredes et al. (1991) as well as to the typical velocity of the disc flow. The adiabatic expansion, which is mainly important for synchrotron emission, does not affect much the emission mechanism mentioned here. The rise time of bubble emission is assumed to be ~ 1 day.

4.3. Comparison with the Results

The observational upper limits are compared with light curves calculated from the model. The energy thresholds of our results have been scaled to 1 TeV assuming a $E^{-2.0}$ spectrum. The spectra calculated with the model assumption (i) in disc-pulsar wind interaction, are integrated (E $\geq$ 1 TeV) for four different mass outflow parameters, $x_{\rm disc} = 500$, 1000, 1500, and 5000 (Fig. 6). The outflow parameter is constrained by our results to $x_{\rm disc} \leq$1500. The light curves with the different model assumptions (i)–(iii) for the fixed mass outflow parameter $x_{\rm disc}$ of 1500 are shown in Fig. 7. As discussed in the previous subsection, the light curve is reduced by a factor of $\sim 10^{-2}$ outside the assumed disc–pulsar-wind interaction period since the polar-wind becomes the only counterpart of the pulsar-wind. In addition, contribution from the wind-bubble formed in the disc–pulsar-wind interaction, remains while the bubble is moving in the disc. Thus, for the model assumption (iii) where the disc and the pulsar-wind interact twice in the orbit, the emission peak after periastron consists of the "second" disc–pulsar-wind interaction, of the disc-wind-bubble interaction where the bubble is the outcome of the "first" interaction, and of the polar-wind–pulsar-wind interaction. For all three assumptions the constraint from the observations, mainly from *Obs. A*, is similar. With this relatively small outflow pressure, the Be star wind may not be able to overwhelm the pulsar wind pressure to produce accretion onto the pulsar, as has been suggested by the X-ray observations.

Besides our emission models based on the Be-star outflows, we discuss the light curve shown in Fig. 5 of Ball & Kirk (2000) as the optimum case for TeV emission from the pulsar wind side, using rather ideal model of the inverse Compton scattering on the un-shocked pulsar wind with a wind Lorentz factor of 10^7. Our upper limits are modified into units of integral energy flux using approximated spectral indices in Fig. 4 of Ball & Kirk (2000),

but the obtained limit of $\sim 1 \times 10^{-5}$MeVcm^{-2}s^{-1}, does not strongly constrain the model since the light curve quickly declines from $\sim$5 at the periastron epoch to 0.2 in units of 10^{-5}MeVcm^{-2}s^{-1}. The integrated flux greater than 1 TeV is obtained from another model calculation of pulsar wind emission using the spectra in Fig. 7 of Murata et al. (2003). They argue for the dominance of synchrotron cooling in the energy loss of the pulsar wind electrons. Assuming the distance of 1.5 kpc, the predicted flux of 10^{-14}cm^{-2}s^{-1} is about two orders of magnitude smaller than our limit.

Recently, new projects of ground based Cherenkov telescopes have begun operations (Ong 2003). With the improved sensitivity and the lower energy threshold, they will offer a better opportunity to observe the PSR B1259−63 binary system in the high-energy band. For projects such as CANGAROO-III or H.E.S.S., located in the southern hemisphere, a 50-hour observation of the binary system gives a typical sensitivity of $\sim 10^{-11}$cm^{-2}s^{-1} with the energy threshold of $\sim$100 GeV (Konopelko 1999). The calculated spectra of our models are integrated again, for the energy greater than 100 GeV, for comparison with this sensitivity. In Fig. 8, the sensitivity levels of 20-hour, 10-hour and 5-hour (statistically scaled) observations, respectively, are drawn over the calculated light curves. A day-scale light curve might be detectable for the model with $x_{\rm disc} \geq \sim$700 along the periastron passage. Ball & Dodd (2001) estimate the $\sim$100 GeV emission from the pulsar wind with a Lorentz factor of 10^6, and their light curves are compared with these expected sensitivities after modification of the unit into the integral energy flux (MeVcm^{-2}s^{-1}), assuming the spectral shape (Fig. 4 of Ball & Dodd (2001)). The light curves in Fig. 8 (*right*) are taken from Fig. 5 of Ball & Dodd (2001) showing terminated (solid line) and un-terminated (dashed line) shock models in the pulsar wind emissions. Both model predictions are comparable with the detectable flux, at least, around the periastron epoch. From Murata et al. (2003), integrations $E \geq 100$ GeV are performed resulting in fluxes of $\sim 4 \times 10^{-12}$cm^{-2}s^{-1} at periastron and $\sim 1 \times 10^{-12}$cm^{-2}s^{-1} at apastron, which is still below the improved sensitivity of ground based detectors.

5. Summary

The PSR B1259−63/SS2883 binary system has been observed at TeV energies using the CANGAROO-II 10-m telescope. The observations were performed at two different orbital phases following the October 2000 periastron. Upper limits on the integrated TeV gamma-ray flux are obtained. A new model for gamma-ray emission from the Be star outflow has been introduced, and contributions from Bremsstrahlung, inverse Compton scattering, and proton-proton interactions, are calculated, with possible variations in parameters considered. The light curves are calculated with different assumptions on the disc-pulsar wind interaction.

The estimated light curves are discussed and compared with our observational results to constrain the disc-like outflow density $\rho_{0,-12} = \rho_0/10^{-12}$ g cm^{-3} and its flow speed $v_{0,6} = v_0/10^6$ cm s^{-1} by $x_{\rm disc} = \rho_{0,-12}\ v_{0,6} \leq 1500$. The next periastron will occur in March 2004 when the condition will favorable for small zenith angle observations and hence low energy thresholds for ground based Cherenkov telescopes. Further observations of PSR B1259−63 system during the periastron passage (including the weeks before and after the periastron, respectively) are encouraged to provide valuable information.

The authors greatly thank Dr. L. Ball for introducing his model calculations to us and for promoting the first idea of these observations. Dr. T. Terasawa gave useful comments in the early discussion of the model. The research was supported by a Grant-in-Aid for Scientific Research of the Ministry of Education, Culture, Science, Sports and Technology of Japan and by the Australian Research Council. AA, SH, JK, LK, KO, KS, and KT were supported by Research Fellowship and Postdoctoral Fellowships of Japan Society of Promotion of Science.

REFERENCES

Asahara, A. et al. 2003, Nucl. Inst. Meth., submitted

Ball, L., Melatos, A., Johnston, S. & Skjaeraasen O. 1999, ApJ, 514, L39

Ball, L. & Kirk, J. G. 2000, Astropart. Phys., 12, 335

Ball, L. & Dodd, J. 2001, Publ. Astron. Soc. Aust., 18, 98

Baring, M. G., Ellison, D. C., Reynolds, S. P., Grenier, I. A., & Goret, P. 1999, ApJ, 513, 311

Cominsky, L., Roberts, M., & Johnston, S. 1994, ApJ, 427, 978

Connors, T. W., Johnston, S., Manchester, R. N., & McConnell, D. 2002, MNRAS, 336, 1201

Cote, J. & Waters, L. B. F. M. 1987, A&A, 176, 93

Dougherty, S. M., Waters, L. B. F. M., Burki, G., Cote, J., Cramer, N., van Kerkwijk, M. H., & Taylor A. R., 1994, A&A, 290, 609

Enomoto, R. et al. 2002, Astropart. Phys., 16, 235

Enomoto, R. et al. 2002, Nature, 416, 823;

Gaisser, T. K., Protheroe, R. J. & Stanev, T., 1998, ApJ, 492, 219

Grove, J. E., Tavani, M., Purcell, W. R., Johnson, W. N., Kurfess, J. D., Strickman, M. S. & Arons, J., 1995, ApJ, 447, L113

Hillas, A. M., 1982, J. Phys. G 8, 1475

Hirayama, M., Nagase, F., Tavani, M., Kaspi, V. M., Kawai, N. & Arons, J. 1996, PASJ, 48, 833

Hirayama, M., Cominsky, L. R., Kaspi, V. M., Nagase, F., Tavani, M., Kawai, N. & Grove, J. E. 1999, ApJ, 521, 718

Itoh, C. et al., 2003, A&A, 402, 443

Johnston, S., Lyne, A. G., Manchester, R. N., Kniffen, D. A., D'Amico, N., Lim, J. & Ashworth, M. 1992, MNRAS, 255, 401

Johnston, S., Manchester, R. N., Lyne, A. G., Bailes, M., Kaspi, V. M., Guojun, Qiao & D'Amico, N. 1992, ApJ, 387, L37

Johnston, S., Manchester, R. N., Lyne, A. G., Nicastro, L. & Spyromilio, J. 1994, MNRAS, 268, 430

Johnston, S., Manchester, R. N., Lyne, A. G., D'Amico, N., Bailes, M., Gaensler, B. M. & Nicastro, L. 1996, MNRAS, 279, 1026

Johnston, S., Manchester, R. N., McConnell, D. and Campbell-Wilson, D. 1999, MNRAS, 302, 277

Kaspi, V. M. et al., 1995, ApJ, 453, 424

Kaspi, V. M. 1997, in Proc. Neutron Stars and Pulsars, eds.: Shibazaki, N., Kawai, N., Shibata, S. & Kifune, T. (Tokyo: UAP), 519

Kawachi, A. et al. 2001, Astropart. Phys., 14, 261

Kennel, C. F. & Coroniti, F. V. 1984, ApJ, 283, 694

Kirk, J. G., Ball, L. & Skjaeraasen, O. 1999, Astropart. Phys., 10, 31

Konopelko, A. 1999, Astropart. Phys., 11 263

Lamers, H. J. G. L. M. & Waters, L. B. F. M. 1987, A&A, 182, 80

Melatos, A., Johnston, S. & Melrose, D. B. 1995, MNRAS, 275, 381

Müller, D. et al., 1995, in Proc. 24th Internat. Cosmic Ray Conf., (Rome), vol.3 13

Murata, K., Tamaki, H., Maki, H. & Shibazaki, N. 2003, PASJ, 55, 467

Mori, M. et al., 2001, in Proc. 27th Internat. Cosmic Ray Conf., (Hamburg), vol.5 2831

Naito, T. & Takahara, F. 1994, J. Physics. G, 20, 477

Okumura, K. et al., 2002, ApJ, 579, L9

Ong, R. A. 2003, in Proc. The Universe Viewed in Gamma-Rays, eds.: Enomoto, R., Mori, M., & Yanagita, S. (Chiba: UAP), 587

Paredes, J. M., Mart, J., Estallela, R. & Sarrate, J. 1991, A&A, 248, 124

Punch, M. et al., 1992, Nature 358, 477

Sako, T. et al. 1997, in Proc. 25th Internat. Cosmic Ray Conf., (Durban), vol.3 193

Sturner, S. J., Skibo, J. G., Dermer, C. D. & Mattox, J. R., 1997, ApJ490, 619

Tanimori, T. et al. 1998, ApJ, 492, L33

Tavani, M., Arons, A. & Kaspi, V. M. 1994, ApJ, 433, L37

Tavani, M. & Arons, J. 1997, ApJ, 477, 439

Waters, L. B. F. M. 1986, A&A, 162, 121

Waters, L. B. F. M., Taylor, A. R., van den Heuvel, E. P. J., Habets, G. M. H. & Persi, P. 1988, A&A, 198, 200

Wex, N., Johnston, S., Manchester, R. N., Lyne, A. G., Stappers, B. W. & Bailes, M. 1998, MNRAS, 298, 997

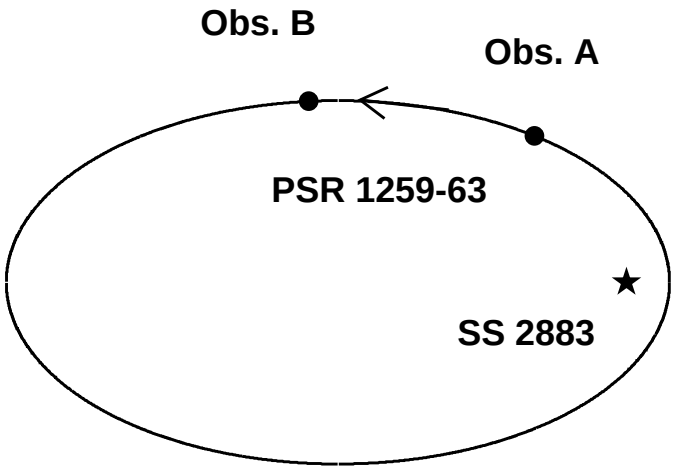

Fig. 1.— Approximate location of the pulsar at the observed orbital phases for *Obs. A* (December 2000) and *Obs. B* (March 2001) are marked as filled circles on the schematic orbit.

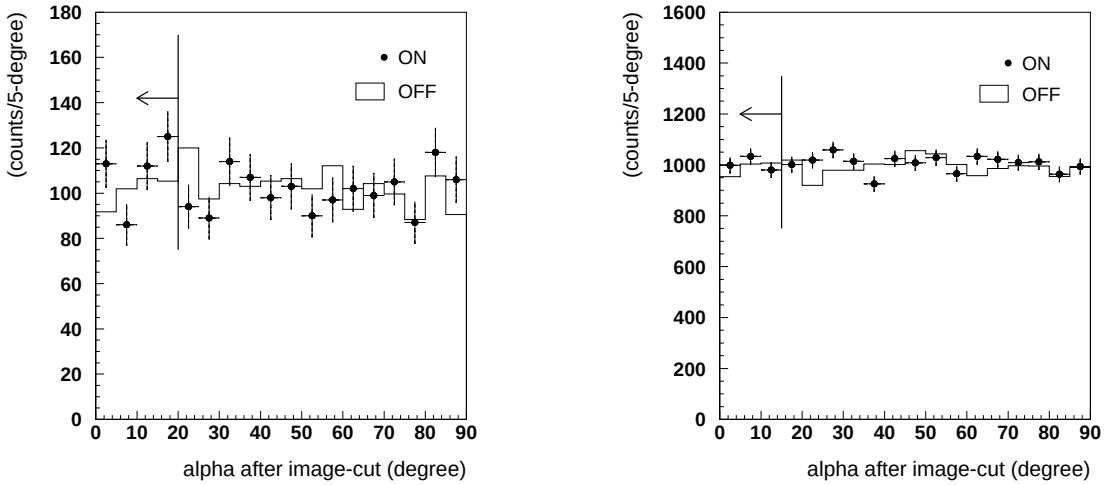

Fig. 2.— Distributions of the orientation angle *alpha*. "OFF" (blank histogram) and "ON" (filled circles with statistical errors) are plotted after normalization. The region $\alpha \leq \alpha_{cr}$ is assumed to contain gamma-ray signals from the binary. $(left) : Obs.\, A$ data set. $\alpha_{cr} = 20°$. $(right) : Obs.\, B$ data set. $\alpha_{cr} = 15°$.

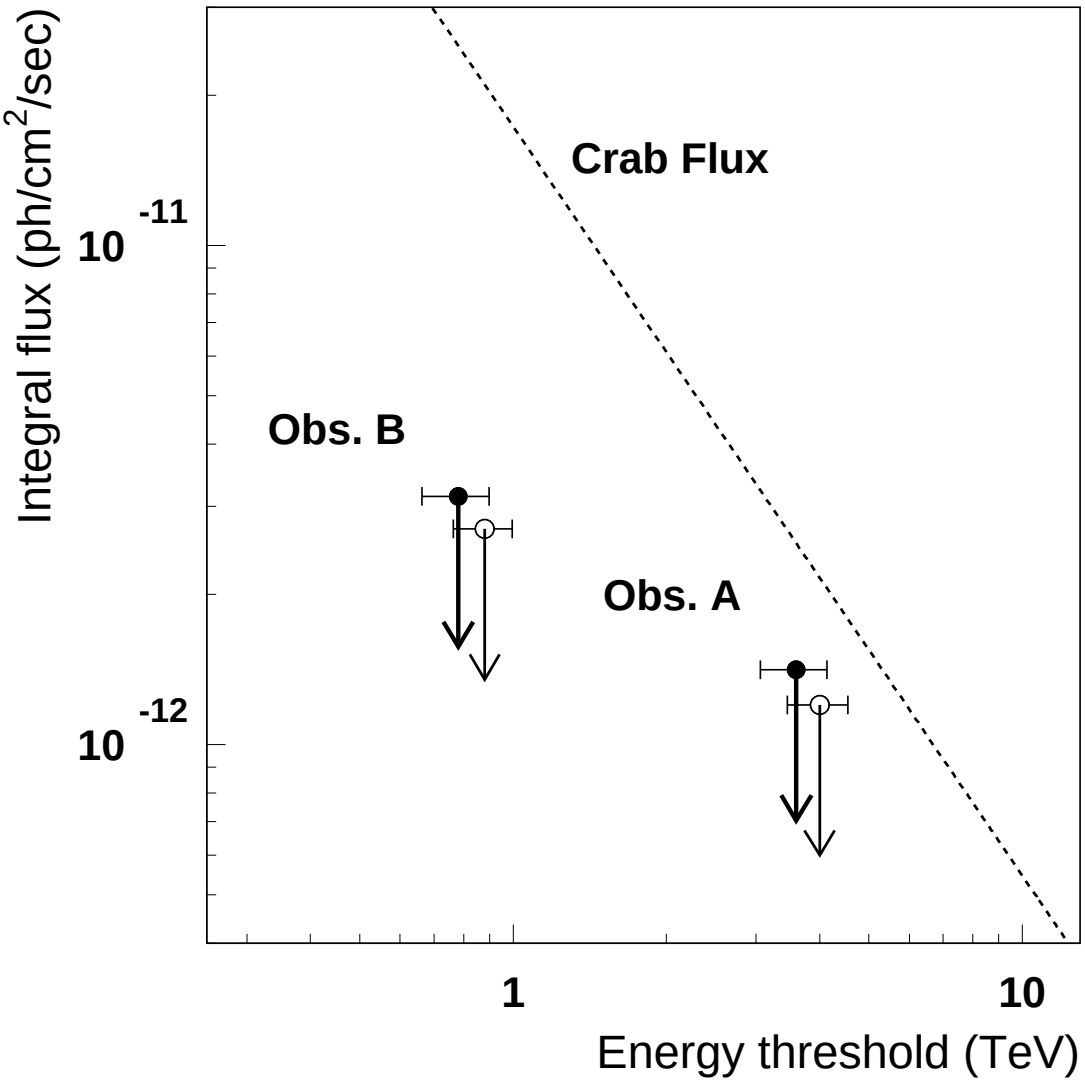

Fig. 3.— Obtained 2-σ upper limits of the integral flux from CANGAROO-II observations. The two observation data sets ($Obs.\,A$ and $Obs.\,B$) have different energy thresholds corresponding to the different zenith angles of the observations. The results obtained assuming a power-law spectral index of -2.5 in the Monte Carlo simulations, are plotted in closed circles, and these with a spectral index of -2.0 are shown in open circles. The integral flux of the Crab nebula, calculated from the differential flux (Tanimori et al. 1998) is plotted for comparison.

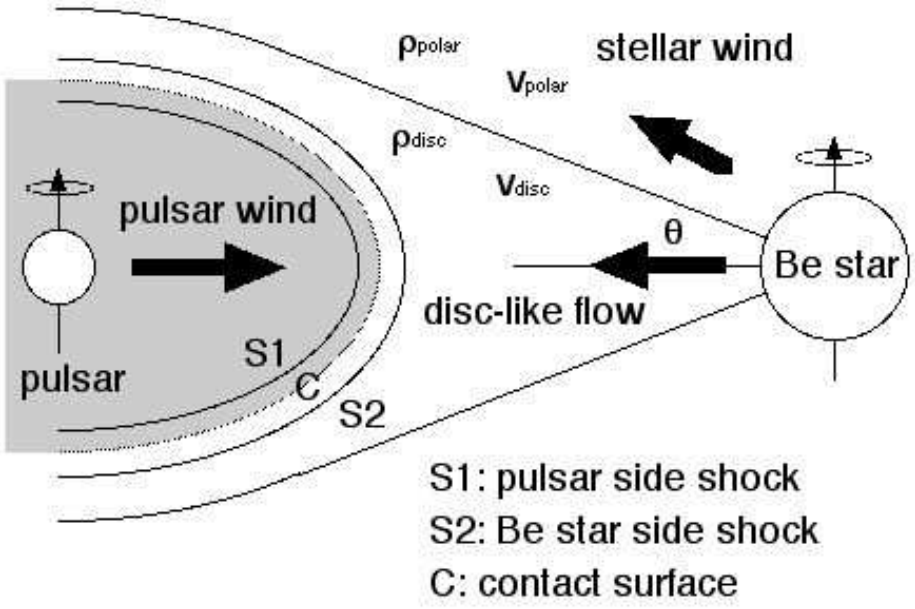
ρpolar
stellar wind
Vpolar
ρdisc
Vdisc
pulsar wind
θ
Be star
disc-like flow
S1
pulsar
C
S2
S1: pulsar side shock
S2: Be star side shock
C: contact surface

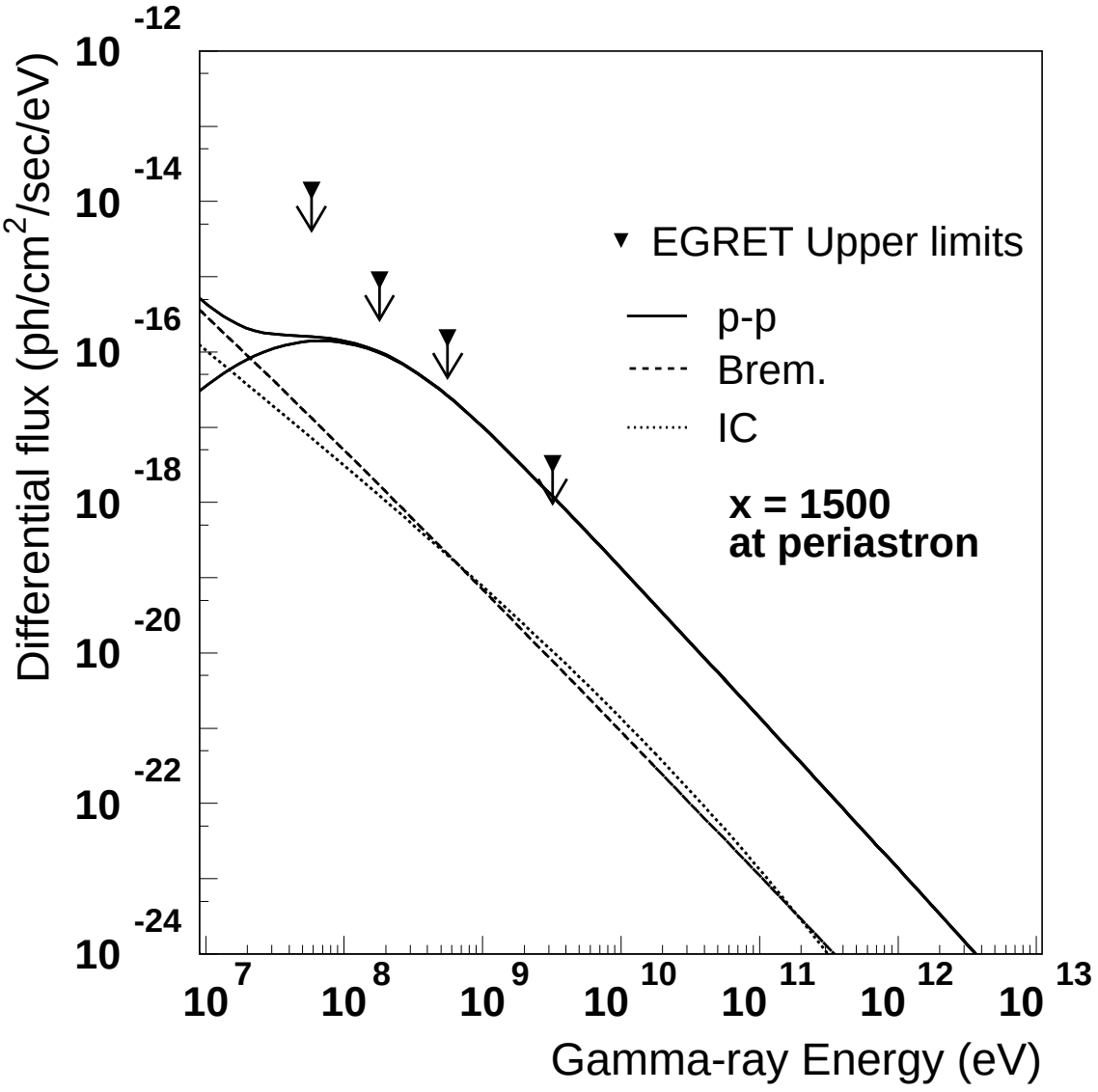

Fig. 5.— Differential flux of the periastron epoch is calculated with $x_{\rm disc} = 1500$, to be compared with the upper limits by *EGRET* at the periastron passage in January 1994 (Tavani & Arons 1997). The contributions from proton-proton collisions (p-p), Bremsstrahlung (Brem.), inverse Compton scattering (IC), and the total flux are shown.

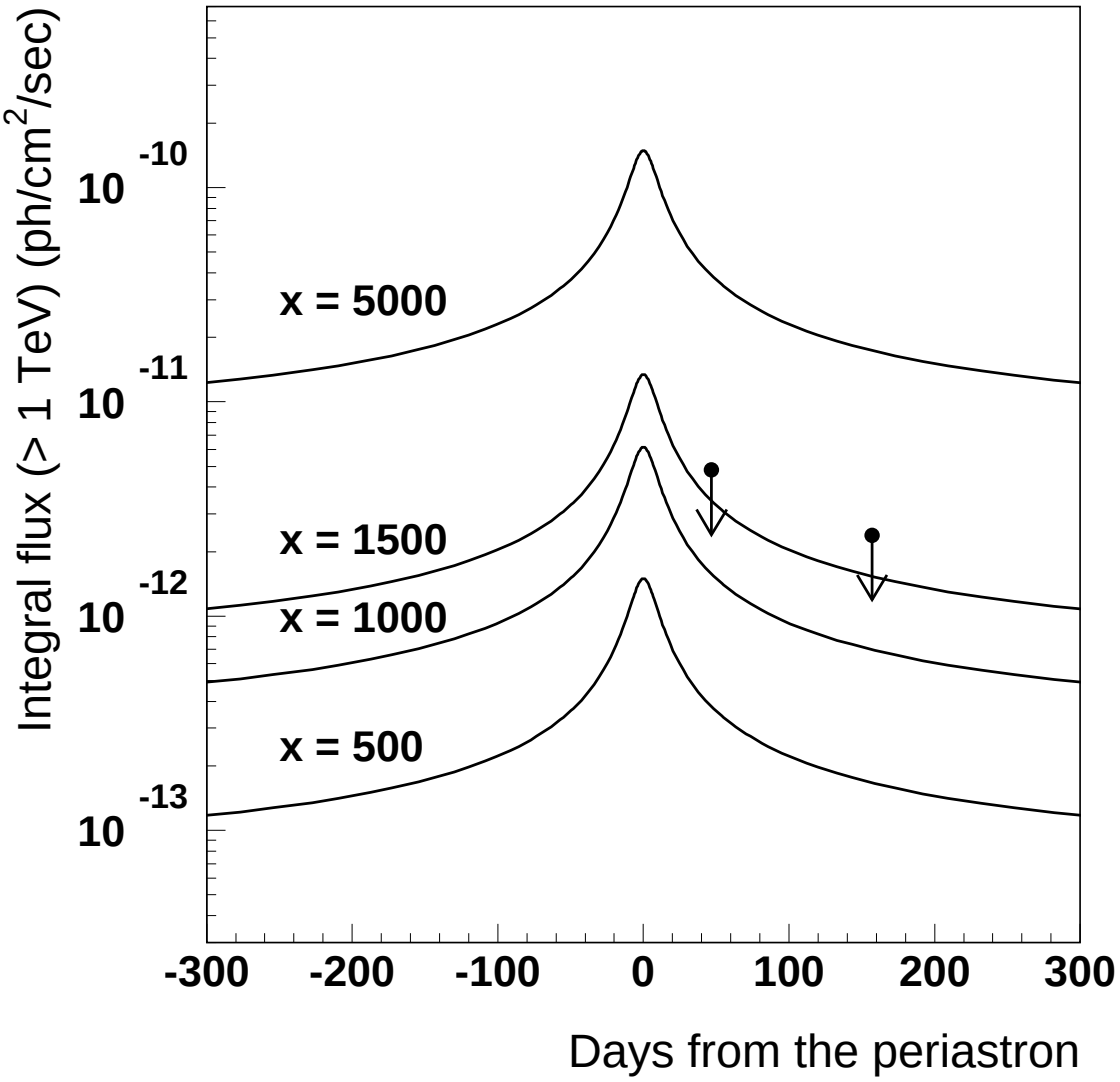

Fig. 6.— Upper limits on the integrated gamma-ray flux are compared with the model calculated curves (E $\geq$ 1 TeV) as a function of days from periastron epoch. The energy thresholds of our results have been scaled to 1 TeV assuming a $E^{-2.0}$ spectrum for comparison with the predictions. The light curves of the combined flux from the Be star outflows are calculated with the model assumption (i) (see the text) and $x_{\rm disc}$ = 500, 1000, 1500, and 5000.

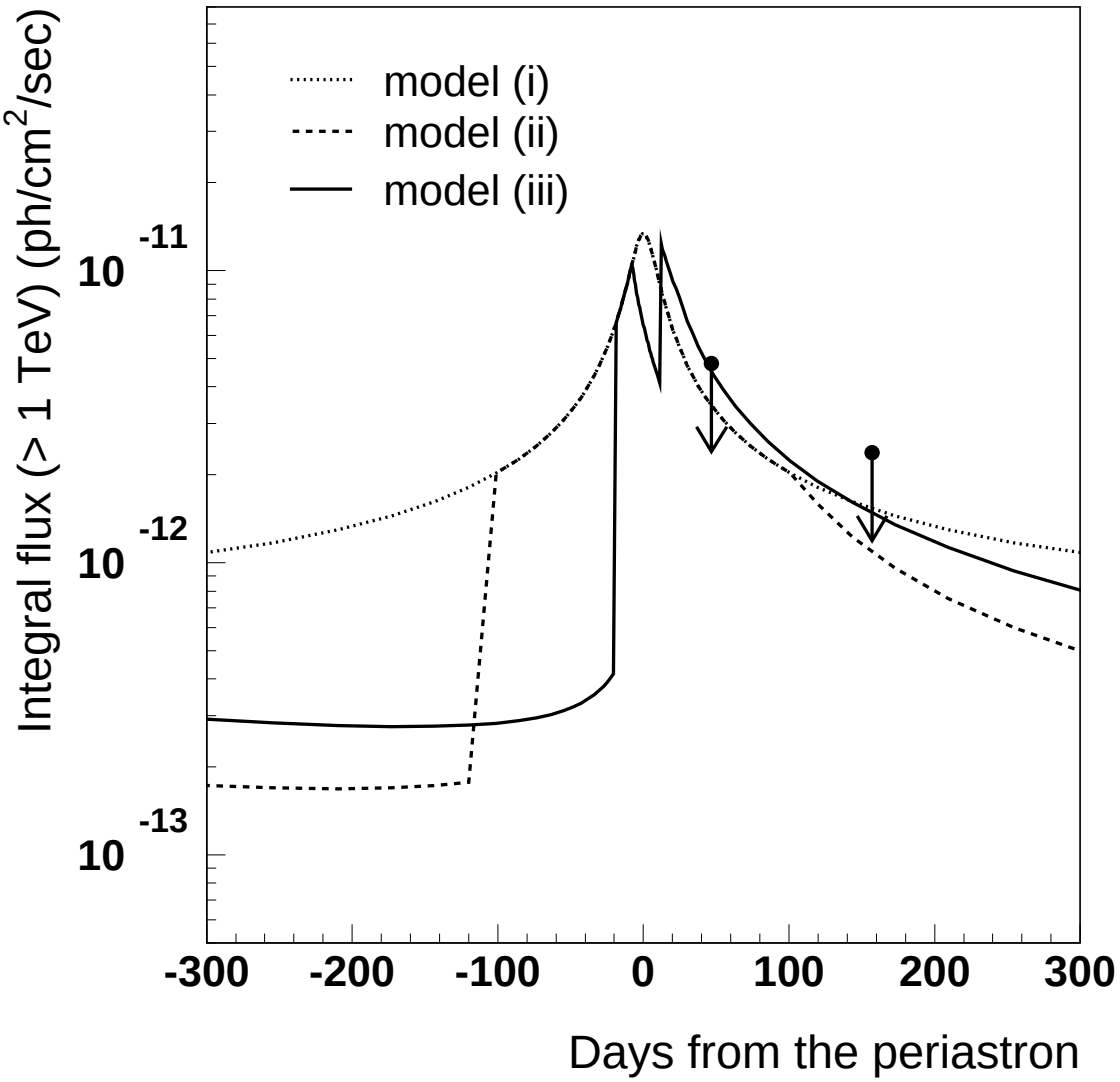

Fig. 7.— Our upper limits and the model calculated light curves ($E \geq 1\,\mathrm{TeV}$) are compared as in Fig. 6. The light curves with x_{disc} of 1500 are calculated with the model assumptions (i)–(iii); where (ii) and (iii) the disc and the pulsar wind are assumed to interact only for the limited period(s).

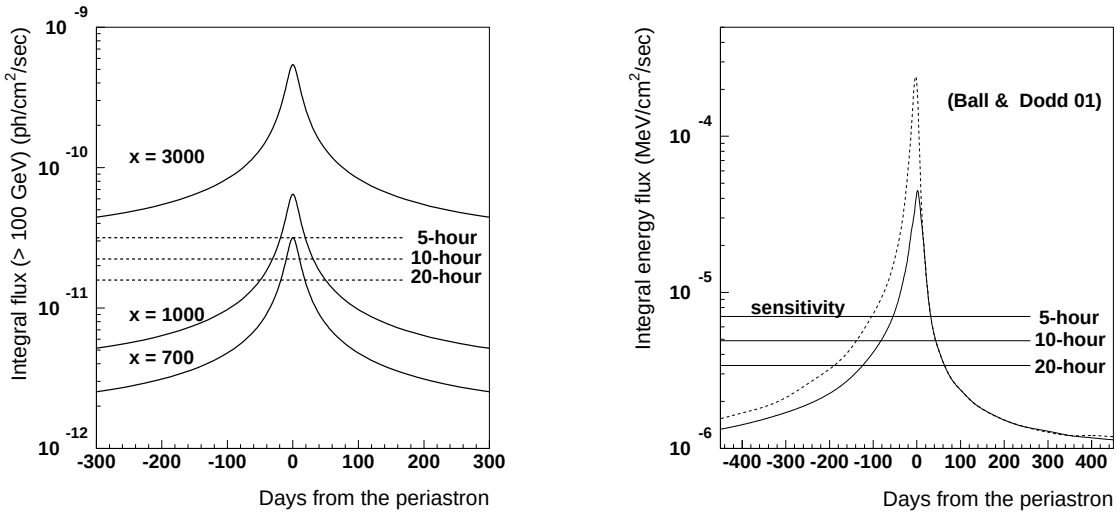

Fig. 8.— The expected sensitivities of the state-of-art Cherenkov telescopes are compared with the models. $(left)$: Corresponding to the improved sensitivity, light curves of our model are re-calculated changing the integral limits, from 1 TeV to 100 GeV. The sensitivity levels of 20, 10, and 5-hour observations are drawn in dotted lines. $x_{\rm disc}$ of 700, 1000 and 3000 are tried. $(right)$: The estimated light curves of 100 GeV emissions from the pulsar wind are taken from Fig. 5 of Ball & Dodd (2001). Calculated results for the terminated and un-terminated pulsar wind models are shown in solid and dotted lines, respectively. The unit of the expected sensitivities (20, 10, and 5-hour) are modified in MeVcm^{-2}s^{-1}, using the approximated spectral shape of Fig. 4 of Ball & Dodd (2001).

Table 1: CANGAROO-II observations of the PSR B1259−63/SS2883 binary. The days after the October 2000 periastron are calculated with the average MJD of the observation periods.

Observation	Epoch		True Anomaly[a]	Separation[b]
	(UT)	(MJD)	(degree)	(10^{13}cm)
Obs. A				
	2000/12/01	51879.72–51879.76		
	2000/12/03	51881.69–51881.74		
	2000/12/04	51882.71–51882.76		
	ave. 51881.4, periastron + 47 days		125	3.6
Obs. B				
	2001/03/19	51987.60–51987.68		
	2001/03/21	51989.62–51989.75		
	2001/03/22	51990.62–51990.79		
	2001/03/24	51992.59–51992.73		
	2001/03/25	51993.54–51993.70		
	2001/03/26	51994.53–51994.60		
	ave. 51991.5, periastron + 157 days		153	8.1

[a]The true anomaly is zero at the epoch of periastron

[b]The binary separation at periastron is assumed to be 0.97×10^{13}cm

Table 2: Summary of the observations and the data reduction. In the effective observation time, data taken in poor weather conditions have been rejected and the dead-time due to the data acquisition process has been corrected for. The cuts applied to the camera images are described in the text. The average zenith angle θ_{zen} is calculated for the whole observation set. The energy threshold E_{th} has been deduced assuming a spectral index of -2.5 and is identical in the ON- and OFF-source data.

Data	θ_{zen}	E_{th}	Time		Number of events		
			Real	Effective	Recorded	Noise Reduction	Image Selected
	(degree)	(TeV)	(min)	(min)			
Obs. A							
ON:	58.9	3.6	202	196	1.17E5	6.62E3	1.85E3
OFF:	59.2		193	160	4.29E5	5.86E3	1.62E3
Obs. B							
ON:	34.0	0.78	1078	623	4.43E6	7.06E4	1.81E4
OFF:	34.3		1001	645	2.63E6	7.21E4	1.87E4

Table 3: Adopted parameters in the model calculation of gamma-ray emissivity. See the text for the detailed definitions.

Parameters	Adopted Values
Pulsar wind :	
Fraction to the equatorial plane, f_{pw}	0.1
Be star :	
Radius, R_*	$6R_\odot = 4.17 \times 10^{11}$cm[a]
Distance, D	1.5 kpc[a]
Opening angle of the disc outflow, θ_{disc}	15 degree
Power law index of density profile of the disc, n_{disc}	2.5
Power law index of density profile of the polar wind, n_{polar}	2
Efficiency of the acceleration, f_{acc}	0.1 (proton)
	0.001 (electron)
Power law index of the proton/electron energy flux, α	-2.0
Maximum energy of the accelerated particles, $E_{e,p}^{max}$	10^{15} eV
Outflow parameter of the disc, x_{disc}	500 – 5000
Outflow parameter of the polar wind, x_{polar}	$10^{-1} \times x_{disc}$

[a]Taken from Johnston et al. (1994)